

**AD-A282 951**



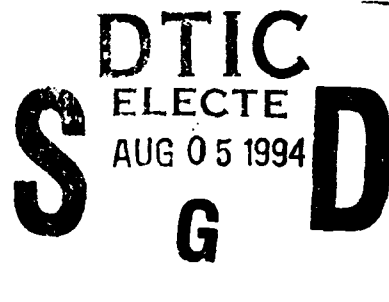
**WL-TR-94-3023**

**THE BEHAVIOR OF LINEAR RECONSTRUCTION TECHNIQUES ON  
UNSTRUCTURED MESHES**

**Michael Aftosmis, Datta Gaitonde and T.Seen Tavares  
Flight Dynamics Directorate  
Wright Laboratory  
Wright-Patterson Air Force Base, OH 45433**

**February 1994**

**Final Report for Period January 1993 - January 1994**



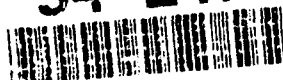
**Approved for public release; distribution is unlimited.**

**FLIGHT DYNAMICS DIRECTORATE  
WRIGHT LABORATORY  
AIR FORCE MATERIEL COMMAND  
WRIGHT-PATTERSON AIR FORCE BASE, OHIO 45433-7562**

**DTIC QUALITY INSPECTED 8**

**94 8 04 \* 05 8**

**94-24730**



*STP*


**9**

## NOTICE

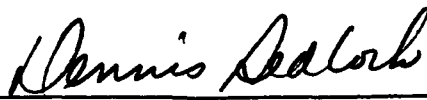
When Government drawings, specifications, or other data are used for any purpose other than in connection with a definitely Government-related procurement, the United States Government incurs no responsibility or any obligation whatsoever. The fact that the government may have formulated or in any way supplied the said drawings, specifications, or other data, is not to be regarded by implication, or otherwise in any manner construed, as licensing the holder, or any other person or corporation; or as conveying any rights or permission to manufacture, use, or sell any patented invention that may in any way be related thereto.

This report is releasable to the National Technical Information Service (NTIS). At NTIS, it will be available to the general public, including foreign nations.

This technical report has been reviewed and is approved for publication.

  
MICHAEL J. AFTOSMIS  
Aerospace Engineer  
Wright Laboratory/NASA Ames  
Research Center

  
JOSEPH M. MANTER  
Chief  
CFD Research Branch

  
DENNIS SEDLOCK  
Acting Chief  
Aeromechanics Division

If your address has changed, if you wish to be removed from our mailing list, or if the addressee is no longer employed by your organization please notify WL/FINE, WPAFB, OH 45433-7562 to help us maintain a current mailing list.

Copies of this report should not be returned unless return is required by security considerations, contractual obligations, or notice on a specific document.

REPORT DOCUMENTATION PAGE			Form Approved OMB No. 0704-0188	
Public reporting burden for this collection of information is estimated to average 1 hour per response, including the time for reviewing instructions, searching existing data sources, gathering and maintaining the data needed, and completing and reviewing the collection of information. Send comments regarding this burden estimate or any other aspect of this collection of information, including suggestions for reducing this burden, to Washington Headquarters Services, Directorate for Information Operations and Reports, 1215 Jefferson Davis Highway, Suite 1204, Arlington, VA 22202-4302, and to the Office of Management and Budget, Paperwork Reduction Project (0704-0188), Washington, DC 20503.				
1. AGENCY USE ONLY (Leave blank)	2. REPORT DATE 1 February 1994	3. REPORT TYPE AND DATES COVERED Final Report Jan 93 - Jan 94		
4. TITLE AND SUBTITLE The Behavior of Linear Reconstruction Techniques on Unstructured Meshes		5. FUNDING NUMBERS PE:61101 PR:2405 TA:T5 WU:00		
6. AUTHOR(S) Michael Aftosmis Datta Gaitonde T. Sean Tavares				
7. PERFORMING ORGANIZATION NAME(S) AND ADDRESS(ES) Flight Dynamics Directorate (WL/FIMC) Wright Laboratory Air Force Materiel Command Wright-Patterson AFB OH 45433-7562		8. PERFORMING ORGANIZATION REPORT NUMBER  WL-TR-94-3023		
9. SPONSORING / MONITORING AGENCY NAME(S) AND ADDRESS(ES) Michael Aftosmis, (415) 604-4499 Flight Dynamics Directorate (WL/FIMC) Wright Laboratory Air Force Materiel Command Wright-Patterson AFB OH 45433-7562		10. SPONSORING / MONITORING AGENCY REPORT NUMBER  WL-TR-94-3023		
11. SUPPLEMENTARY NOTES				
12a. DISTRIBUTION / AVAILABILITY STATEMENT  Approved for public release; distribution unlimited.		12b. DISTRIBUTION CODE		
13. ABSTRACT (Maximum 200 words)  This report presents an assessment of a variety of reconstruction schemes on meshes with both quadrilateral and triangular tessellations. The investigations measure the order of accuracy, absolute error and convergence properties associated with each method. Linear reconstruction approaches using both Green-Gauss and least squares gradient estimation are evaluated against a structured MUSCL scheme wherever possible. In addition to examining the influence of polygon degree and reconstruction strategy, results with three limiters are examined and compared against unlimited results when feasible. The methods are applied on quadrilateral, right triangular, and equilateral triangular elements in order to facilitate an examination of the scheme behavior on a variety of element shapes. The numerical test cases include well known internal and external inviscid examples and also a supersonic vortex problem for which there exists a closed form solution to the 2-D compressible Euler equations. Such investigations indicate that the least squares gradient estimation provides significantly more reliable results on poor quality meshes. Furthermore, limiting only the face normal component of the gradient can significantly increase both accuracy and convergence while still preserving the integral cell average, and maintaining monotonicity. The first order method performs poorly on stretched triangular meshes, and analysis shows that such meshes result in poorly aligned left and right states for the Riemann problem. The higher average valence of a vertex in the triangular tessellations does not appear to enhance the wave propagation, accuracy, or convergence properties of the method. Typically, quadrilateral elements provide superior or equivalent discrete solutions with approximately 50% fewer edges in the domain (2-D). However, on very poor quality meshes, the triangular elements routinely yield superior accuracy as a result of the trapezoidal quadrature of the Galerkin portion of the numerical flux function.				
14. SUBJECT TERMS  Unstructured, Upwind, Inviscid, reconstruction, Limiters, Riemann problems		15. NUMBER OF PAGES 51		
		16. PRICE CODE		
17. SECURITY CLASSIFICATION OF REPORT Unclassified	18. SECURITY CLASSIFICATION OF THIS PAGE Unclassified	19. SECURITY CLASSIFICATION OF ABSTRACT Unclassified	20. LIMITATION OF ABSTRACT UL	

# Contents

<b>List of Figures</b> . . . . .	iv
<b>Acknowledgements</b> . . . . .	v
<b>1 Introduction</b> . . . . .	1
<b>2 Theoretical Model</b> . . . . .	4
2.1 Formulation . . . . .	4
2.2 Limiters . . . . .	9
2.3 Flux Quadrature . . . . .	11
<b>3 Results and Investigations</b> . . . . .	13
3.1 Convergence and Efficiency . . . . .	13
3.1.1 Convergence . . . . .	15
3.1.2 A Note on Efficiency . . . . .	17
3.2 Order of Accuracy and Absolute Error . . . . .	17
3.2.1 Supersonic Vortex . . . . .	17
3.2.2 Polygon Degree . . . . .	21
3.2.3 Limiter Behavior . . . . .	26
3.2.4 Polygon Quality . . . . .	30
3.3 External Inviscid Flow - Transonic NACA 0012 Airfoil . . . . .	37
<b>4 Conclusions</b> . . . . .	41
<b>5 References</b> . . . . .	43

Accession For	
NTIS	CRA&I <input checked="" type="checkbox"/>
DTIC	TAB <input type="checkbox"/>
Unannounced <input type="checkbox"/>	
Justification .....	
By .....	
Distribution /	
Availability Codes	
Dist	Avail and / or Special
A-1	

## List of Figures

1	Unstructured triangular mesh surrounding vertex $V_0$ . . . . .	5
2	Physical mesh and median dual for quadrilateral, right triangular and equilateral triangular tessellations showing support for gradient calculation at control volume surrounding node $V_0$ .	8
3	Density contours for supersonic, inviscid flow through channel with 4% circular arc. $M_\infty = 1.4$ , $65 \times 17$ mesh.	14
4	Convergence histories for various schemes on each mesh for supersonic inviscid flow through channel with 4% circular arc. $CFL = 0.75$	16
5	Sequences of regular meshes used for supersonic vortex . . . . .	19
6	Pressure contours on medium meshes with various reconstruction methods and limiters. $M_{in} = 2.25$ , $\rho_{in} = 1$ , $p_{in} = 1/\gamma$ , $r_i = 1$ , $r_o = 1.384$	20
7	Contours of density error on medium meshes for supersonic vortex test case. Contours drawn every 2%. $M_{in} = 2.25$ , $\rho_{in} = 1$ , $p_{in} = 1/\gamma$ , $r_i = 1$ , $r_o = 1.384$	22
8	Order of accuracy of unlimited schemes on regular meshes for the supersonic vortex problem	24
9	Setting up of the local Riemann problem on a face of the auxiliary meshes for quadrilateral and right triangular tessellations	25
10	Order of accuracy of limited schemes on regular polygons for the supersonic vortex problem	29
11	Sequences of stretched meshes used for supersonic vortex . . . . .	31
12	Order of accuracy of limited schemes on stretched polygons for the supersonic vortex problem	32
13	Sequences of randomly distorted meshes used for supersonic vortex . . . . .	34
14	Order of accuracy of limited schemes on randomly distorted polygons for the supersonic vortex problem	35
15	Meshes and isobars for a sampling of typical discrete solutions for a NACA 0012 at $M_\infty = 0.8$ and $\alpha = 1.25$ deg. (upper - quadrilaterals, lower - triangles, $131 \times 65$ mesh)	38
16	$C_p$ distributions with various schemes for Mach 0.8, $\alpha = 1.25^\circ$ NACA 0012 airfoil	40

## **Acknowledgements**

The authors would like to thank T.Barth, V.Venkatakrishnan, M.Berger and W.K.Anderson for many insightful discussions and suggestions over the course of this research. The Numerical Aerodynamic Simulation Facility at NASA Ames provided computing support for much of this work, and this support is gratefully acknowledged.

# 1. Introduction

The recent success of characteristic-based upwind differencing on structured meshes has spawned significant research into adopting such methods for use in unstructured adaptive mesh flow solvers [1–4]. Several basic approaches for the construction of characteristic based unstructured flow solvers have evolved in recent years. To first order, the support stencils employed in most of these methods are similar in that they rely only on next-neighbor information in a manner which mimics first order structured schemes. The essential difference in the design of these methods lies in their extension to higher order spatial accuracy.

One approach towards obtaining higher order begins with constructing what is essentially the structured difference stencil on the unstructured mesh. References [2,4], for example, use either Harten's modified flux approach [5] or van Leer's MUSCL [6] reconstruction to obtain higher order accuracy. Such schemes typically make use of one additional point beyond the nearest neighbor in their difference stencils. Passing this information through the unstructured mesh is the essential challenge faced in their design and implementation. This noncompactness introduces additional complexity into the methods and usually requires additional storage to overcome. A main benefit of this approach is that the resulting schemes generally retain the favorable convergence, robustness, and accuracy properties associated with upwind schemes on structured meshes [2].

A second technique was introduced by Ref. [1] using a centered approximation for estimation of the slope within each control volume, and thus obtains higher order accuracy without informational inquiries beyond the nearest neighbor. The Green's theorem approach adopted by Barth's linear reconstruction [1] essentially degenerates to the Fromm scheme in one-dimension [7]. Variations on this theme have been proposed by Ref. [3] and others. Additionally, the concept of using a nearest-neighbor based slope estimation was immediately generalized to use least squares, constrained least squares, and higher-order procedures [8–10].

Relying only upon next-neighbor information maintains a compactness comparable to central difference based schemes and permits the use of edge-based — and other compact — data structures. A main strength of this class of methods, is that they avoid the ambiguities associated with the mapping of structured mesh based difference stencils onto an unstructured mesh and data structure [11].

A second important strength stems from the divestment of the gradient calculation from the stencil associated with the Riemann solver. The method requires only a best estimate of the solution gradient within each control volume, and while the surface integral used in linear reconstruction still suffers on poor quality meshes, more elaborate gradient estimations may not. Such procedures may provide dramatically more reliable gradient estimates and suggests the possibility of constructing schemes with much greater tolerance for poor quality meshes. This point becomes increasingly important when considering viscous simulations [12]. In such cases, accurate evaluations of the second derivatives often place severe restriction on the quality of acceptable meshes, and the high aspect ratio cells necessary to resolve the stiff physics of high Reynolds number viscous flow may actually hinder accurate gradient estimates. One goal of the present work is to examine the scheme behavior in detail on the right triangular meshes often employed to resolve viscous layers.

An abundance of research in the recent literature has attempted to capitalize on the promises of various reconstruction techniques. Nevertheless, outstanding questions concerning convergence, accuracy, robustness, and monotonicity remain. The present effort focuses on the simulation of inviscid flow with Roe's approximate Riemann solver. Time integration is achieved via a three-stage modified Runge-Kutta method. The investigations are specifically designed to examine the accuracy, stability and expense of the various reconstruction algorithms and comparisons with structured MUSCL schemes are provided wherever possible. The methods are examined on meshes consisting of quadrilateral, right triangular, and equilateral triangular elements to examine the effects of polygon shape on convergence and accuracy. Both Green-Gauss and least squares



reconstructions are considered using Barth's original Limiter [1], Venkatakrishnan's limiter [7] and a new directional limiter which is presented in Section 2 of this paper.

The investigations are designed to independently examine the methods in a controlled setting. In addition to several well known numerical test cases, these examples also include problems for which there exist closed form solutions to the 2-D compressible Euler equations. Such cases facilitate quantitative statements about scheme performance and order of accuracy.

## 2. Theoretical Model

The governing equations are written in flux-integral form:

$$\int \int_A \frac{\partial}{\partial t} \vec{U} dA = - \oint_S \vec{F} \cdot \vec{n} dS \quad (2.1)$$

where  $\vec{U}$  is the state vector of conserved variables and  $\vec{F}$  is the tensor of flux density containing the inviscid components of the Navier-Stokes equations. This equation may be discretized on an unstructured mesh containing polygons of arbitrary degree. Figure 1 shows a small region of a typical mesh with triangular elements. The present work adopts a node-based approach and thus the flow variables reside at the mesh vertices. The solution procedure for Equation 2.1 consists of reconstruction, flux quadrature and updating of the state variables. The flux quadrature requires evaluation of a divergence operator while the reconstruction step necessitates estimation of a gradient.

### 2.1 Formulation

We begin by deriving the edge formulas for the reconstruction as in Ref. [13]. This is useful since the analysis contained in subsequent sections will examine many of these expressions and assumptions in significant detail. In Figure 1, the perimeter of the polygon formed by the set of triangles containing  $V_0$  as a common vertex forms the closed path of integration  $S$ . The polygon enclosed by this boundary has an area,  $A$ , equal to the sum of the areas of the figures which share the common vertex  $V_0$ . Thus, the integral path for any given point is chosen to be that described by joining all adjacent points as defined by the edge to edge connections. Applying Green's theorem in the plane then provides an evaluation of the gradient of a passive scalar  $\phi$  at the vertex  $V_0$ ,

$$\int \int_A \nabla \phi dA = \oint_S \phi \hat{n} dS \quad (2.2)$$

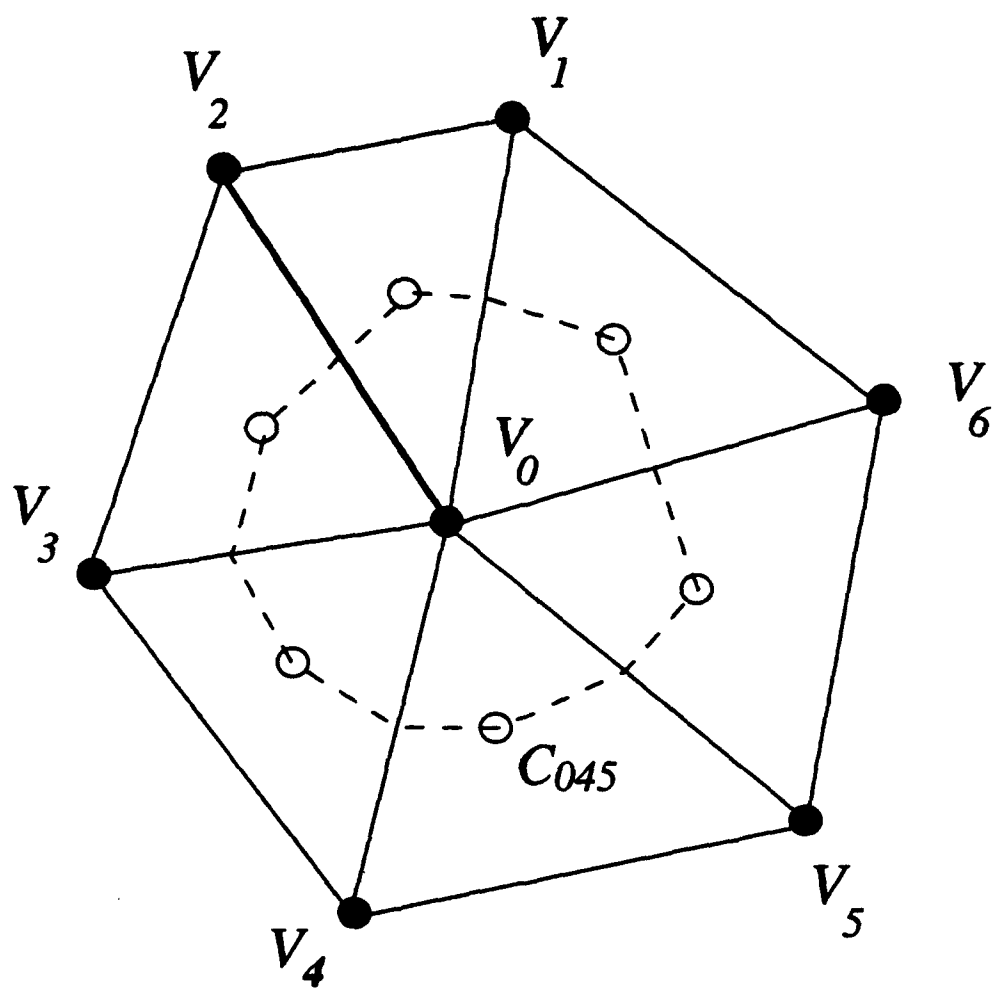


Figure 1: Unstructured triangular mesh surrounding vertex  $V_0$

where  $\hat{n}$  denotes the outward facing local unit normal to  $S$ . On the multifaceted control volume shown in Figure 1, the trapezoidal rule provides a discrete analog to Equation 2.2 and is exact if  $\phi$  is linear. The contribution of each edge  $V_i V_j$  to the gradient of  $\phi$  at  $V_0$  is then:

$$\frac{1}{2} (\phi_{V_i} + \phi_{V_j}) \vec{n}_{V_i V_j} \quad (2.3)$$

where  $i, j$  vary cyclically,  $i, j \in \{1, 2, \dots, 6\}$  and  $\vec{n}_{V_i V_j}$  denotes the surface normal vector to edge  $V_i V_j$ . Following Ref. [13], separation of the cell based formula in Equation 2.3 into contributions from each of the edges incident upon  $V_0$  permits reexpressing the integration on an edge-basis, and so, the trapezoidal evaluation of the path integral in Equation 2.2 may be equivalently expressed in terms of contributions associated with each node. For a vertex  $V_j$  on the perimeter of the cell surrounding vertex  $V_0$ , this term is

$$\frac{1}{2} \phi_{V_j} (\vec{n}_{V_i V_j} + \vec{n}_{V_j V_k}) \quad i, k \text{ are vertices adjacent to } j \quad (2.4)$$

To further facilitate application in an edge-based setting, the vectors in Equation 2.4 may be written in terms of edges of the centroid dual without changing the actual path of integration  $S$  in Equation 2.2. Ref. [8] points out

$$\vec{n}_{V_i V_j} + \vec{n}_{V_j V_k} = 3\vec{n}_{C_{0ij} C_{0jk}} \quad (2.5)$$

where  $C_{ijk}$  denotes the centroid of the triangle formed by vertices  $V_i, V_j, V_k$ . The quadrature of Equation 2.2 is evaluated with Equations 2.3 through 2.5 to obtain:

$$\int_A \nabla \phi dA = \oint_S \phi \vec{n} dS = \sum_{j \in V_1, \dots, V_6} \phi_{V_j} \frac{3}{2} \vec{n}_{C_{0ij} C_{0jk}} \quad (2.6)$$

with  $i, k$  once again denoting the vertices adjacent to  $j$ . Hence, the gradient at  $V_0$  may be written as

$$(\nabla \phi)_{V_0} = \frac{3}{A} \sum_{j \in \{V_1, \dots, V_6\}} \frac{1}{2} \phi_{V_j} \vec{n}_{C_{0ij} C_{0jk}} \quad (2.7)$$

To further simplify the operations, Equation 2.7 can be made symmetric with respect to the contribution of the vertices associated with each edge. This is achieved by noting that if the surface vectors of the control volume sum to zero, the addition of a constant ( $\frac{1}{2}\phi_{V_0}$ ) to the above formula does not affect the gradient or divergence. Thus, Equation 2.7 may be recast as

$$(\nabla\phi)_{V_0} = \frac{3}{A} \sum_{j \in \{V_1, \dots, 6\}} \frac{1}{2} (\phi_{V_i} + \phi_{V_0}) \vec{n}_{C_{0i,j}C_{0j,k}} \quad (2.8)$$

Finally, since the area  $A_m$  of the median dual is exactly one third that of  $S$ , Equation 2.8 becomes:

$$(\nabla\phi)_{V_0} = \frac{1}{A_m} \sum_{j \in \{V_1, \dots, 6\}} \frac{1}{2} (\phi_{V_i} + \phi_{V_0}) \vec{n}_{C_{0i,j}C_{0j,k}} \quad (2.9)$$

which is the final formula used in the reconstruction.

Minimum-energy or "least squares" reconstruction provides an alternative method for estimating the solution gradient within each cell. This reconstruction process seeks to find the gradient vector which *minimizes the least square error* with respect to the integral cell averages of the *distance one* neighbors. The procedure involves solution of a (usually) overconstrained system of linear equations. The algorithm can be implemented on an edge-by-edge basis at a cost comparable to that of the Green-Gauss formulation. Details of the least squares procedure may be found in Refs. [9], [14], [15] and [16]. As with the Green-Gauss gradient estimation, the set of support vertices for any node includes all distance one neighbors of that node. However, the least squares process generally deemphasizes more distant data as compared to the Green-Gauss method.

Figure 2 contains a quadrilateral, right triangular, and a (nearly) equilateral triangular mesh. This figure displays not only the physical mesh, but also the median duals of each tessellation. These three meshes will be a basis for many of the investigations which follow. In considering the application of Equation 2.9 to unstructured meshes containing polygons other than triangles, consider, for example, its evaluation on quadrilateral cells depicted at the top of Figure 2,

$$(\nabla\phi)_{V_0} = \frac{1}{A_m} \frac{1}{2} \{ \phi_{V_1} \vec{n}_{C_{0187}C_{0123}} + \phi_{V_3} \vec{n}_{C_{0123}C_{0345}} +$$

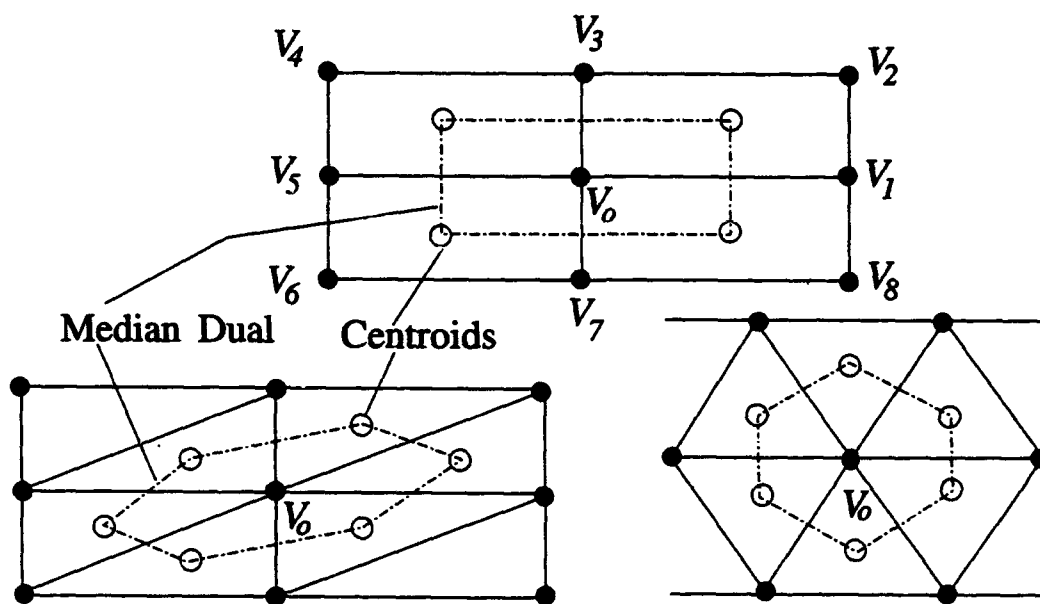


Figure 2: Physical mesh and median dual for quadrilateral, right triangular and equilateral triangular tessellations showing support for gradient calculation at control volume surrounding node  $V_0$ .

$$\phi_{V_5} \vec{n}_{C_{0345}C_{0567}} + \phi_{V_7} \vec{n}_{C_{0567}C_{0187}} \} \quad (2.10)$$

where the contribution of  $\phi_{V_0}$  has been explicitly cancelled. Since the relationship in Equation 2.5 is unique to triangles, this formula corresponds only to a midpoint evaluation of the line integral on the dotted path shown in Figure 2. As a result, some of the favorable properties associated with the trapezoidal integration formula have been sacrificed and slightly less tolerance to mesh irregularities may be expected when using the midpoint formula on quadrilateral control volumes.

Once the gradients of the conserved quantities are known, the scalars may be reconstructed throughout the cell:

$$\phi(x, y) = \phi_{V_0} + \nabla \phi \cdot \vec{r} \quad (2.11)$$

where  $\vec{r}$  is a general vector pointing from  $V_0$  to a point  $(x, y)$ . However, such a procedure will not always yield monotonic behavior. Consequently, a limiter  $\Psi$  is employed to reduce the slope where necessary.

$$\phi(x, y) = \phi_{V_0} + \Psi \nabla \phi|_j \cdot \vec{r} \quad 0 \leq \Psi \leq 1 \quad (2.12)$$

Taking  $\Psi$  identically equal to zero degenerates the algorithm to first order.

## 2.2 Limiters

Barth's [1] original slope limiter is a scalar computed by considering all edges incident upon  $V_0$  and applied directly to  $\nabla \phi$ . Let  $\phi_{r,m}$  be the reconstructed value without limiting at the median point  $V_m$  of edge  $V_0V_j$  using the gradient at  $V_0$ .

$$\phi_{r,m} = \phi_{V_0} + \nabla \phi|_{V_0} \cdot \vec{r}_{V_0V_m} \quad (2.13)$$

Defining  $\phi_{max} = \max(\phi_{V_0}, \phi_{V_j})$ ,  $\phi_{min} = \min(\phi_{V_0}, \phi_{V_j})$ ,  $\Delta_{1,max} = \phi_{max} - \phi_{V_0}$ ,  $\Delta_{1,min} = \phi_{min} - \phi_{V_0}$ ,  $\Delta_2 = \phi_{r,m} - \phi_{V_0}$ , the scalar  $\Psi_{0j}$  associated with the gradient at  $V_0$  due to edge  $V_0V_j$  is

$$\Psi_{0j} = \begin{cases} \min\left(1, \frac{\Delta_{1,max}}{\Delta_2}\right) & \text{if } \Delta_2 > 0 \\ \min\left(1, \frac{\Delta_{1,min}}{\Delta_2}\right) & \text{if } \Delta_2 < 0 \\ 1 & \text{if } \Delta_2 = 0 \end{cases} \quad (2.14)$$

$\Psi$  is constructed from the various  $\Psi_{0j}$  values:  $\Psi = \min(\Psi_{0j})$  where  $j$  scans all vertices joined to  $V_0$ . This method thus reduces the gradient in all directions equally and pushes Equation 2.12 toward first order in all spatial directions. Such "scalar" limiting reduces both the normal and tangential components of the gradient and results in a relatively dissipative process.

This observation suggests that a less dissipative limiter may be constructed by limiting only the component of  $\nabla\phi$  along the surface vector associated with each edge. A "directional" limiter may be defined in which  $\Psi$  does not act isotropically. We begin by resolving the gradient into components normal ( $\hat{n}$ ) and tangential ( $\hat{\tau}$ ) to an edge of the centroid dual.

$$\nabla\phi = (\nabla\phi \cdot \hat{n})\hat{n} + (\nabla\phi \cdot \hat{\tau})\hat{\tau} \quad (2.15)$$

$\Psi$  is computed in a manner similar to that described above but is now applied only to the component of the gradient normal to the edge of the dual.

$$\nabla\phi = \Psi((\nabla\phi \cdot \hat{n})\hat{n}) + (\nabla\phi \cdot \hat{\tau})\hat{\tau} \quad (2.16)$$

The limited gradient still ensures a new maximum is not created along the edge and yet it now avoids unnecessarily degrading the tangential component of the slope.

In an attempt to further reduce the severity of limiting, a face-based implementation of this directional limiting was examined. With this approach, the limiting is performed locally for each face separately without influencing the gradient stored at the nodes. Thus, the limiting at any one face of a control volume on the dual mesh occurs independently of any limiting which may be necessary on the other faces. This procedure is analogous to that on a structured mesh where the



limiter is applied sequentially in the mesh directions. The process does not preserve the mean of the function value within each cell, but can dramatically diminish the number of flux calculations which invoke the limiter. This face based approach may increase storage requirements somewhat since the limiter must be computed on an edge-by-edge basis. Results with this implementation are unsatisfactory when used in conjunction with Barth's original limiting procedure, and although monotone solutions are produced with low absolute error in one dimension, multidimensional results are erratic. "Face-based" limiting was not investigated in conjunction with other limiting procedures and is not considered further within this work.

Venkatakrishnan [7] recently proposed a new limiter designed specifically to enhance the convergence properties of the base scheme. This increase in convergence comes at the expense of strict monotone behavior, as the new (smooth) limiter permits small local overshoots or undershoots in the discrete solution. This limiter may be expressed as:

$$\psi_{0j} = \begin{cases} \frac{1}{\Delta_2} \frac{(\Delta_{1,max}^2 + \bar{\epsilon}^2) \Delta_2 + 2\Delta_2^2 \Delta_{1,max}}{\Delta_{1,max}^2 + 2\Delta_2^2 + \Delta_{1,max} \Delta_2 + \bar{\epsilon}} & \text{if } \Delta_2 > 0 \\ \frac{1}{\Delta_2} \frac{(\Delta_{1,min}^2 + \bar{\epsilon}^2) \Delta_2 + 2\Delta_2^2 \Delta_{1,min}}{\Delta_{1,min}^2 + 2\Delta_2^2 + \Delta_{1,min} \Delta_2 + \bar{\epsilon}} & \text{if } \Delta_2 < 0 \end{cases} \quad (2.17)$$

Here,  $\epsilon$  is a small number to prevent division by zero while  $\bar{\epsilon}$  is chosen to be a variable that controls the degree of limiting and depends on some estimate of mesh scale ( $\bar{\epsilon}^2 = (K \Delta x)^3$ ).  $\Delta x$  in this formula is defined locally as the diameter of the largest circle which may be inscribed into a particular control volume.

## 2.3 Flux Quadrature

The divergence operator required for the flux quadrature of Equation 2.1 is closely related to the gradient and consequently follows a similar formulation for each component of the equation. The fluxes are computed in the present work with Roe's flux-difference split method at the midpoint of each edge. First, the state of the flow on either side of the midpoint of each edge is constructed

from the known values of the state at each node and the limited gradients computed with the above procedure. The flux function is then evaluated and appropriately scattered and accumulated to form the solution change at each node.

### 3. Results and Investigations

The investigations examine issues of accuracy, convergence and efficiency with respect to variation in the limiter, type of gradient estimation and the degree and quality of the control volumes in the discretized domain. These studies are conducted against a backdrop of widely computed numerical test cases and closed form analytic solutions to the governing equations. In an effort to ensure that the conclusions drawn are general in nature, the numerical examples consider a variety of smooth and nonsmooth internal and external flows. Wherever possible, efforts are made to compare the unstructured results with those from a structured Roe/MUSCL solver.

#### 3.1 Convergence and Efficiency

Supersonic internal flow through a channel with a 4% circular arc bump provides an initial assessment of the convergence properties of the various methods. Convergence behavior shows very little dependence upon the reconstruction procedure and results are only presented using Green-Gauss.

Figure 3 introduces this example through density contours showing the three tessellations of a  $65 \times 17$  mesh. This widely computed test case considers Mach 1.4 freestream flow which enters the duct and sets up an inviscid shock reflection pattern within the domain [17]. The meshes shown in Figure 3 consist of quadrilateral, right triangular, and equilateral triangular elements, and the cases were computed with both 1st order ( $\nabla \phi \equiv 0$ ) upwinding and linear reconstruction with all three of the limiters outlined in Section 2.2.

All the cases were run at a CFL of 0.75 with local time-stepping, and on all the meshes, the diffusive character of 1st order upwind solutions is apparent. While all of the methods capture the overall lambda shock structure within the duct, the resolution of the interaction region near the trailing edge permits discrimination among the higher order discrete solutions. On each of

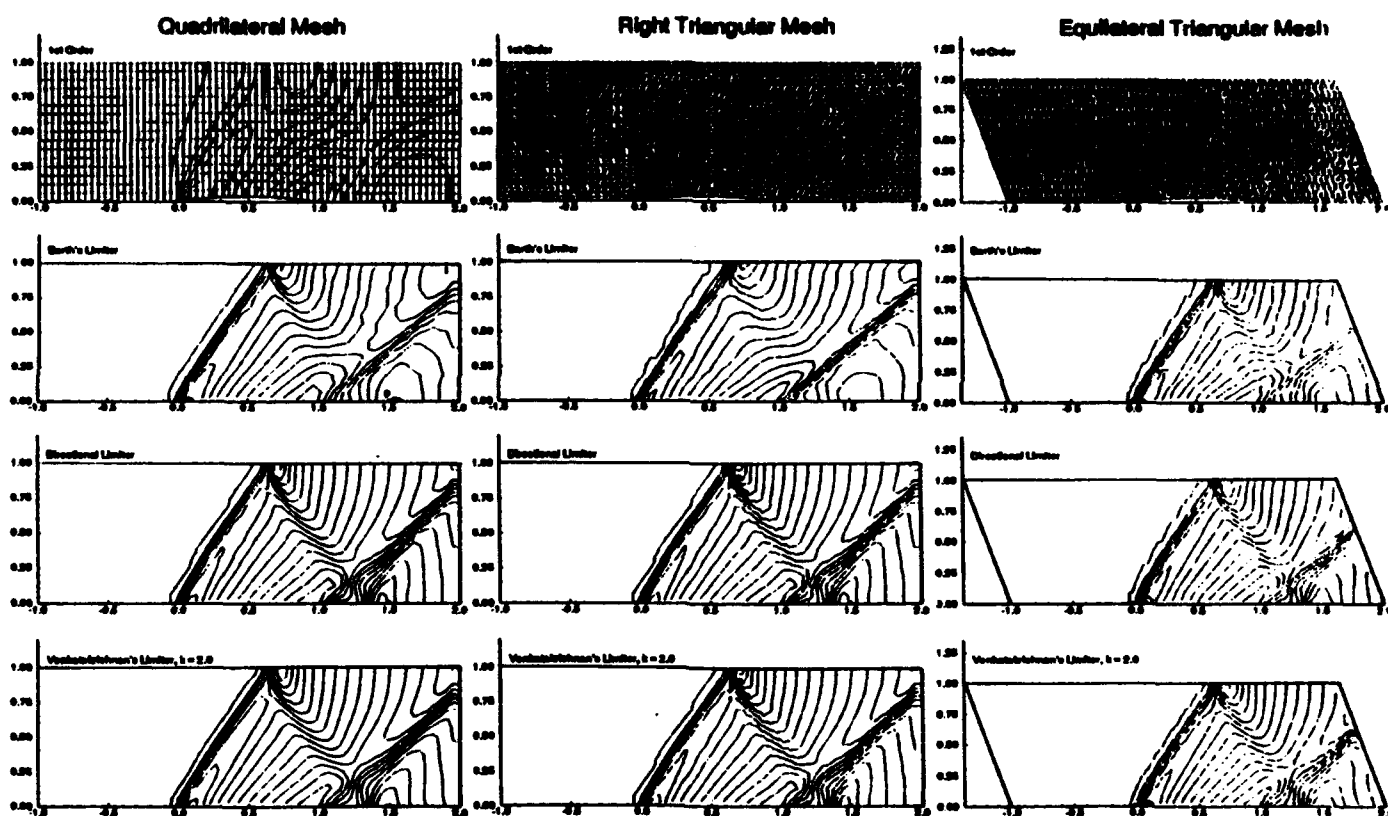


Figure 3: Density contours for supersonic, inviscid flow through channel with 4% circular arc.  $M_\infty = 1.4$ ,  $65 \times 17$  mesh.

the meshes, for example, the directional application of Barth's limiter improves the resolution of this region considerably over the scalar implementation. This is consistent with the observation alluded to in Section 2.2, where it was suggested that limiting only the component normal to the control volume face would result in a less dissipative operator.

Figure 4 shows convergence histories in the  $L_1$  norm for this case on all three meshes. All of the examples with Venkatakrishnan's limiter used a value of the free parameter ( $K$ ) of 2.0. On both triangular meshes, variation of this parameter by more than about  $\pm 0.5$  resulted in poor convergence. Convergence behavior on the quadrilateral meshes did not begin to degenerate until this parameter was increased beyond 5.0.

### 3.1.1 Convergence

Looking strictly at the convergence histories it would at first appear that neither Barth's original limiter nor the directional limiter allow the calculations to converge convincingly. However, an examination of the contour plots at several points in the convergence history revealed that these fluctuations manifest themselves only as small amplitude wiggling of the contours about a steady state as has been reported by other investigations [7]. For the directional limiter, the fluctuations are about an order of magnitude smaller and perturbations of the contour lines are not immediately evident (although undoubtedly there). This is consistent with the results displayed by the convergence histories. The directional limiter enhanced convergence by roughly an additional order of magnitude, obviously indicating less activity.

One plausible explanation for this behavior views these fluctuations in the convergence histories as the results of sporadic firing of the limiter, thus preventing absolute convergence. This assertion is further supported by the work of Ref. [7], where the free parameter ( $K$ ) in Venkatakrishnan's limiter was introduced to prevent the limiter from prematurely reacting to slight oscillations. In the present examples, incorporation of this tolerance facilitates convergence to machine zero on all three meshes (32-bit machine). The directional limiter displays behavior

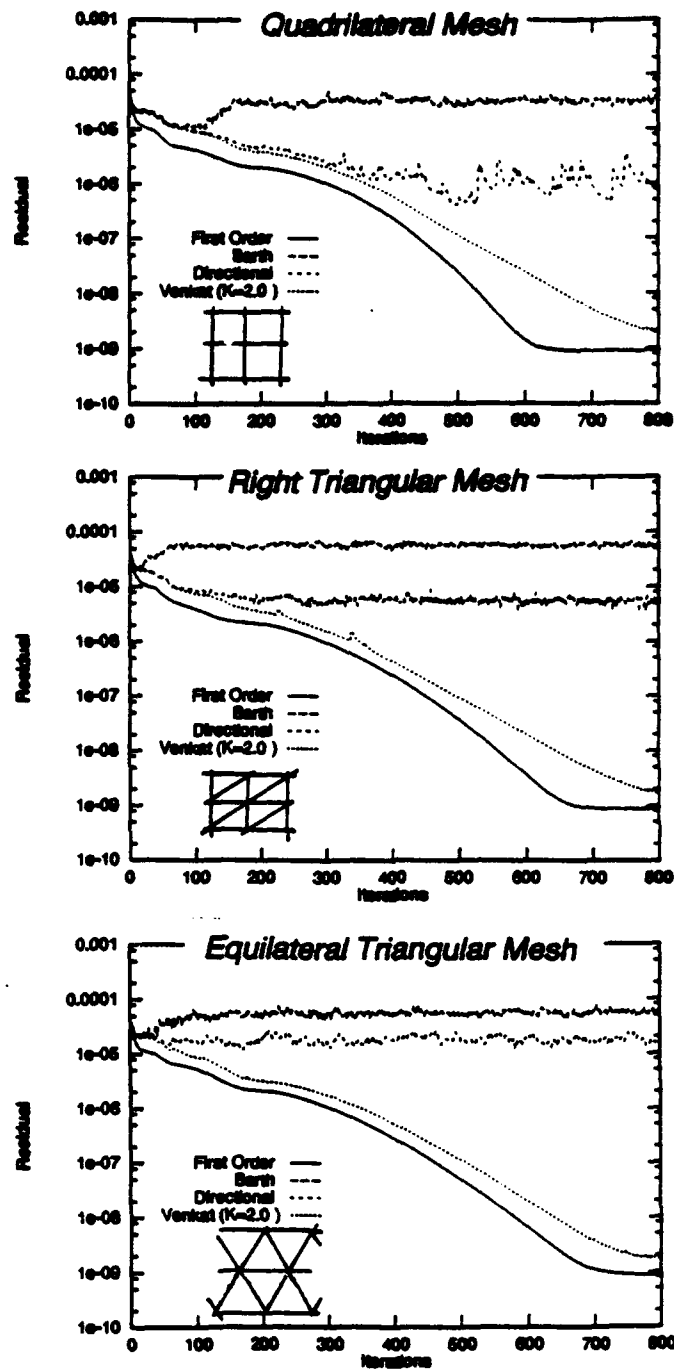


Figure 4: Convergence histories for various schemes on each mesh for supersonic inviscid flow through channel with 4% circular arc.  $CFL = 0.75$

similar to that of Barth. However, in all of the cases , the fact that it only retards one component of the gradient results in somewhat better convergence since the limiting is less severe. This issue will be revisited in the next investigation, where the behavior of each of the limiters is mapped out in detail.

### **3.1.2 A Note on Efficiency**

As a final note, it is worth mentioning that while all three meshes require roughly the same number of iterations to converge, the calculations on the triangular meshes were 50% more expensive in both memory and time than those on the quadrilateral meshes. This follows since the scheme proceeds on an edge-by-edge basis and six edges (instead of four) are incident upon each vertex in the interior of the mesh. In three dimensions, a typical interior vertex has six incident edges on hexahedral meshes, while a corresponding vertex will have approximately 12-14 incident edges on a tetrahedral mesh. Thus, about 2 to 2.5 times times the storage will be needed if a tetrahedral mesh is chosen. The hope is, of course, that the additional edges and flux evaluations in triangular and tetrahedral domains may enhance the wave propagation within the discrete domain and lead to more accurate numerical solutions. Nevertheless, an examination of Figure 3 does not reveal any obvious benefit stemming from the additional edges present in the tessellation, and it is difficult to justify the additional expense based strictly upon accuracy arguments.

## **3.2 Order of Accuracy and Absolute Error**

### **3.2.1 Supersonic Vortex**

While the example in the previous section gives some basis for comparing the methods, quantitative measurement of the order of accuracy and discretization error associated with each scheme is best performed on a test case for which an exact, closed form, analytic solution exists. Exami-

nation of a two dimensional supersonic vortex provides just such an opportunity. Since this is a shock free compressible flow, the measured order of accuracy is not corrupted by limiter action near shocks and the behavior will correspond to what one may expect of each method in smooth regions of the flow. Using this case as a diagnostic tool permits direct examination of the effects of polygons of various shapes and degrees, and also provides an opportunity to study the tolerance of the methods to poor quality meshes.

The inviscid, isentropic, supersonic flow of a compressible fluid between concentric circular arcs presents a flow in which the velocity varies inversely with the radius. This flow is a particularly useful test case for upwind methods since the numerical solutions must propagate infinitesimally weak waves accurately to perform the large turning without disrupting the radial flow distribution or introducing shocks. This flow is also of some practical interest as it has been used as a segment of the flow distribution in designing passages for the supersonic blading of compressors and turbines [18,19], as well as for a supersonic through-flow fan stage [20].

The expression for density  $\rho$  as a function of radius  $r$  is given by:

$$\rho(r) = \rho_i \left[ 1 + \frac{\gamma - 1}{2} M_i^2 \left\{ 1 - \left( \frac{r_i}{r} \right)^2 \right\} \right]^{\frac{1}{\gamma - 1}} \quad (3.1)$$

where  $M_i$  and  $r_i$  are the Mach number and the radius at the inner arc. To evaluate the order of accuracy of each of the methods, a series of discrete solutions to this test case is obtained on the quadrilateral as well as on equilateral and right triangular meshes. For each tessellation, solutions are sought on a set of three telescoping grids with  $31 \times 6$ ,  $61 \times 11$ , and  $121 \times 21$  nodes. The Mach number at the inner radius  $r_i$  is specified at 2.25 and the outer radius  $r_o$  at  $1.384 r_i$ . Figure 5 shows the three sets of regular meshes used in the simulation. For these regular meshes, the aspect ratio is of order 1.

The simulations are initiated by releasing the inlet profile into a nearly evacuated duct and converged to steady state. Figure 6 displays pressure contours (inc.= 0.25) resulting from the computations on the medium meshes. The extreme diffusivity of the first order schemes again



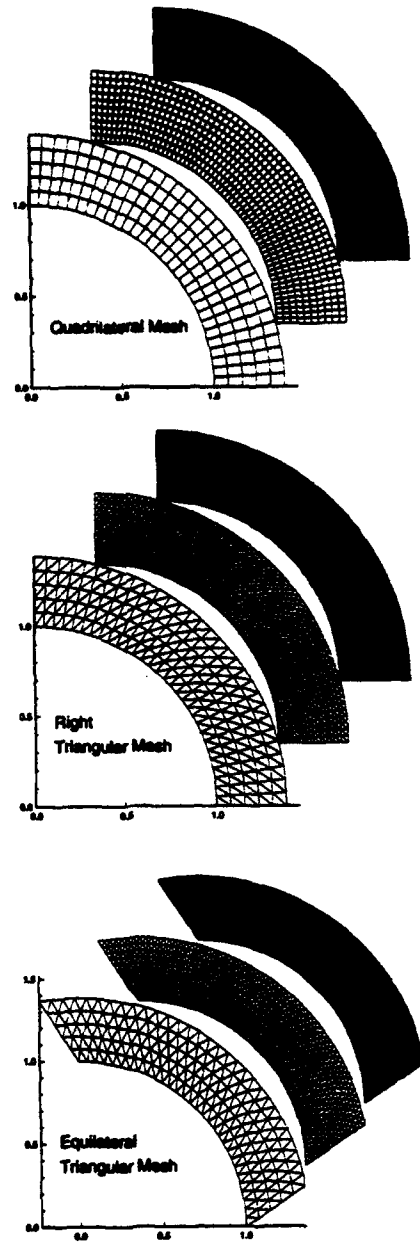


Figure 5: Sequences of regular meshes used for supersonic vortex

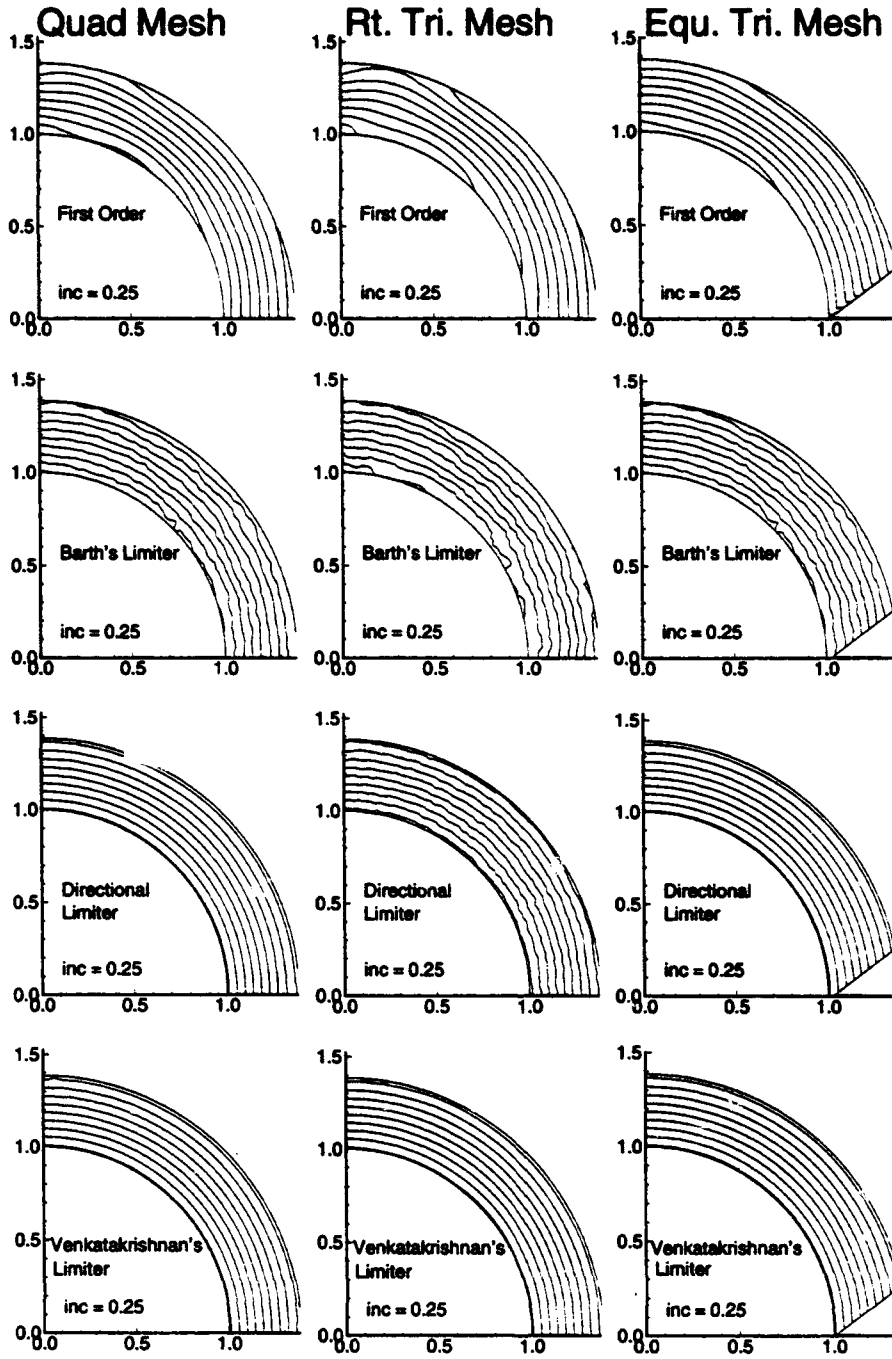


Figure 6: Pressure contours on medium meshes with various reconstruction methods and limiters.  $M_{in} = 2.25$ ,  $\rho_{in} = 1$ ,  $p_{in} = 1/\gamma$ ,  $r_i = 1$ ,  $r_o = 1.384$

becomes apparent in these plots, and the pressure in the first order simulations drops dramatically along stream lines as the flow proceeds around the duct. Some evidence of dissipation is also evident in the higher order discrete solutions but it is not nearly as pronounced as in the first order cases. Convergence behavior for all the schemes mimics that for the duct flow case presented earlier. The noise in the solutions with the first two limiters will be discussed shortly.

The existence of an exact solution to this problem makes it possible to directly compute distributions of error throughout the domain.

Figure 7 contains contour plots of density error for the medium triangular and quadrilateral meshes for all the methods. Each contour level indicates 2% error in the local density distribution. Note that the error contours do not display any anomalies approaching the walls or boundaries, suggesting that the accuracy near the wall is the same as that in the interior of the field.

By comparing the error in the discrete solutions on a successively refined sequence of telescoping meshes, quantitative measurements of both order of accuracy and absolute error are possible. Note that since the simulations were run to convergence, the error measured is not directly truncation error but rather the error in the discrete solutions. The Appendix tabulates the  $L_1$  and  $L_2$  norm of the density error in the discrete solutions on all the meshes considered in this example. In addition, it offers order of accuracy estimates for the procedures on each type of polygon. In general, the  $L_1$  and  $L_2$  norms behave quite similarly, and the order of accuracy of the discrete solutions is roughly the same in using either measure. Since the  $L_2$  norm is more sensitive to extrema, this fact suggests that discretization error is being driven out of the domain uniformly, and supports the contention that the boundaries are free from anomalies. Selected data will be extracted from these tables to aid in the analysis of the following sections.

### 3.2.2 Polygon Degree

The first investigation examines the influence of the shape and degree of the polygons in the domain on the accuracy of the discrete solutions. Since results free from the effects of limiters

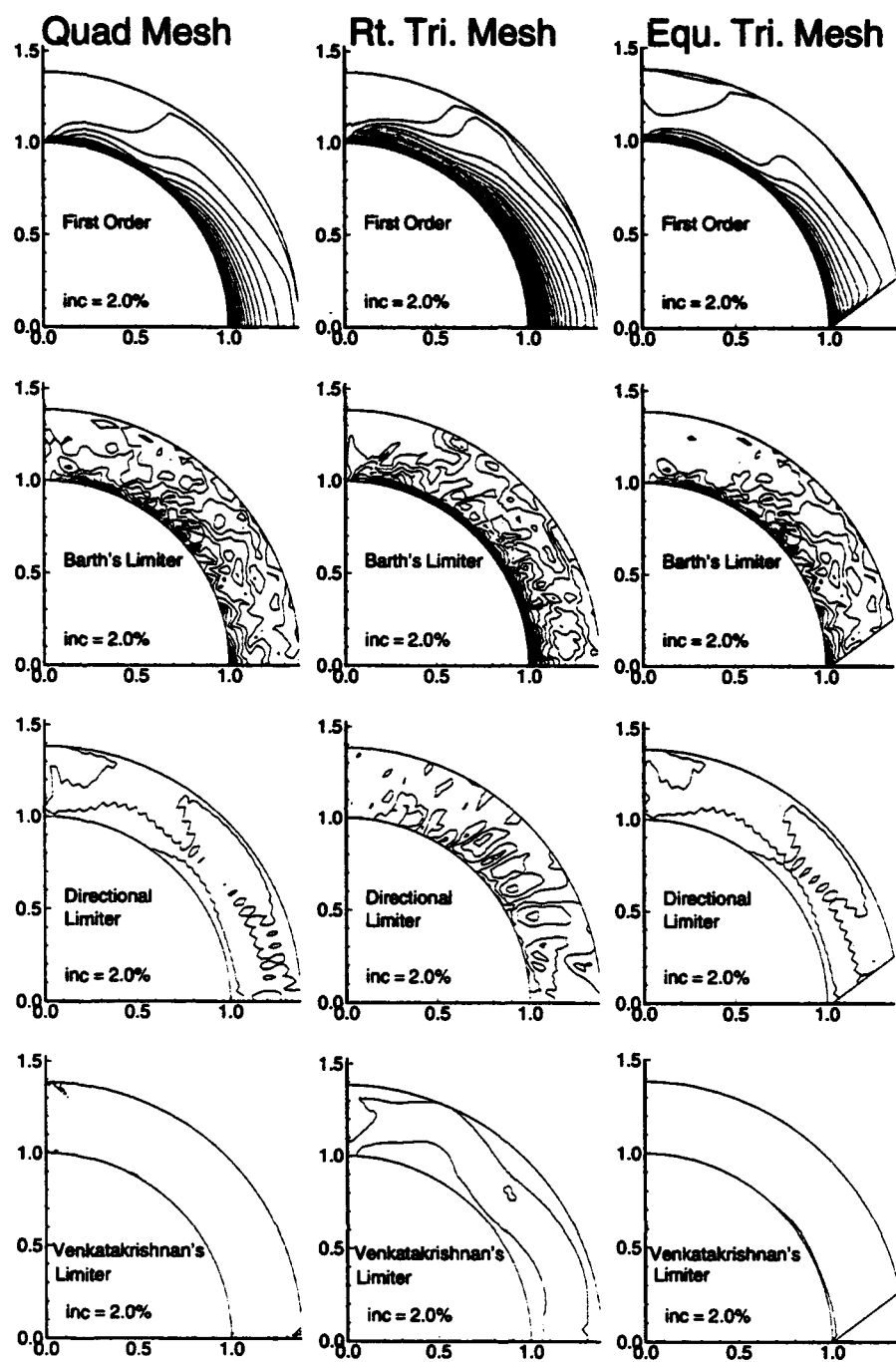


Figure 7: Contours of density error on medium meshes for supersonic vortex test case. Contours drawn every 2%.  $M_{in} = 2.25$ ,  $\rho_{in} = 1$ ,  $p_{in} = 1/\gamma$ ,  $r_i = 1$ ,  $r_o = 1.384$

are sought, the simulations are started from the exact solution, and discrete solutions are obtained without the use of flux limiters. The order of accuracy of the discrete method is assessed by performing a linear regression on log-log plots of absolute density error in both  $L_1$  and  $L_2$  norms versus normalized grid spacing represented by the reciprocal square root of the number of nodes in the domains. Figure 8 presents the order of accuracy of the methods in  $L_1$ , and Table A.1 in the Appendix contains the data used to generate this chart.

In this example, both the order of accuracy, and absolute error on the quadrilateral and equilateral triangular tessellations are comparable. The order of accuracy on these two meshes is 5–10% better than that on the right triangular mesh with either reconstruction procedure. The first order results show a more pronounced deficit, placing the order of accuracy of the right triangular mesh at about 0.7 as compared to 1.1 and 1.0 for the quads and equilateral triangles, respectively. This fact suggests that something in the very nature of the right triangles is responsible for the lower order of accuracy on such meshes.

The sketches in Figure 9 permit a direct comparison of the dual meshes on quadrilateral and right triangular tessellations. In examining this figure it becomes apparent that the face  $a$ , which is pierced by the edge  $LR$  is at a right angle  $\alpha$  on the quadrilateral mesh but not on the stretched triangular mesh. (Note that Figure 2 shows that  $\alpha$  is a right angle on equilateral triangular meshes as well.) In fact, as the mesh stretching increases, the alignment of faces like  $a$ ,  $b$ ,  $d$ , and  $e$  with their respective edges becomes less and less orthogonal.

When the first order essentially 1-D scheme evaluates the flux across a poorly aligned face, like  $a$ , the Riemann solver expects data normal to the face, but the data provided by either vertex of edge  $LR$  is far removed from the true normal, and necessarily introduces an error into the flux evaluation. On unskewed quadrilateral meshes, or equilateral triangular meshes  $\alpha$  is very nearly a right angle. As a result, the data introduced into the approximate Riemann solver is well aligned with the normal to the face, and such an error is avoided. Such arguments support the hypothesis that the first order scheme may degrade rapidly on highly stretched right triangular meshes.

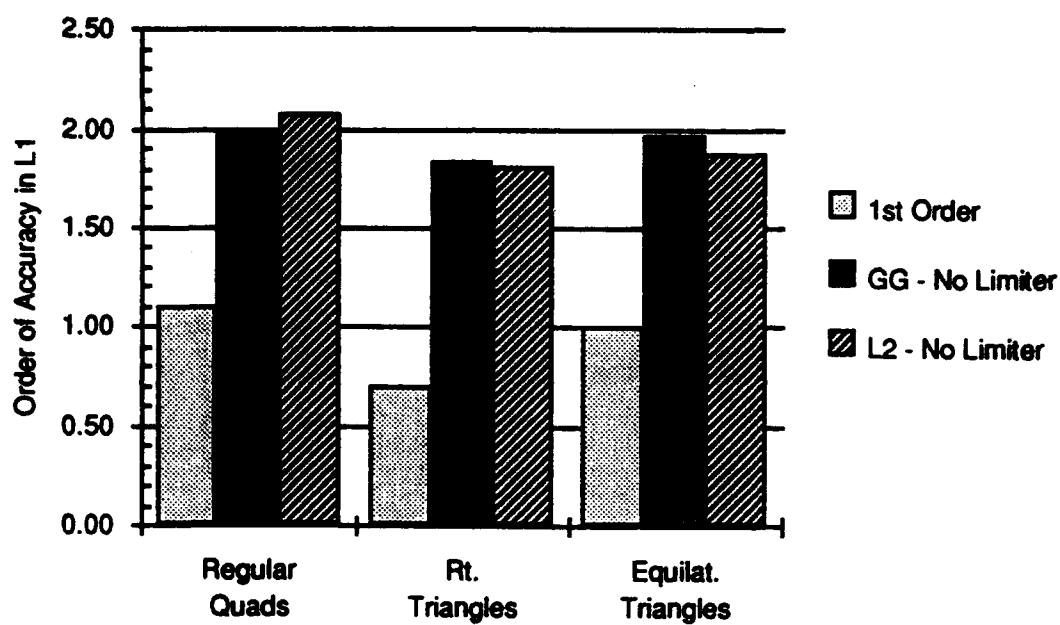


Figure 8: Order of accuracy of unlimited schemes on regular meshes for the supersonic vortex problem

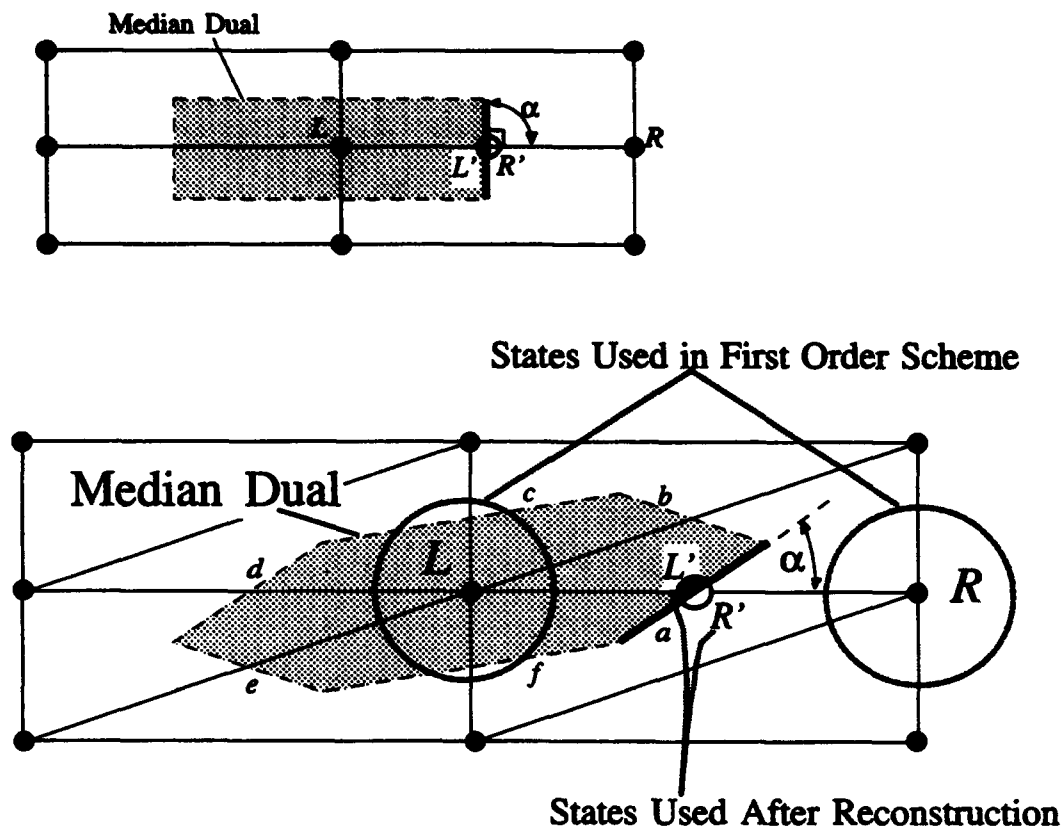


Figure 9: Setting up of the local Riemann problem on a face of the auxiliary meshes for quadrilateral and right triangular tessellations

When linear reconstruction is introduced into the formation of the numerical flux, the new left and right states for the Riemann problem are now formed on either side of face  $a$  in Figure 9. These states are labeled  $L'$  and  $R'$  in the sketch and take into account linear variation within the auxiliary cell. An alternate view of the situation is to realize that the reconstruction step has taken data into account from all of the distance one vertices adjacent to  $L$  and  $R$ , thus enlarging the stencil to permit information to propagate in the face-normal direction. Since there is no direct edge connection normal to face  $a$ , the first order scheme necessarily makes an error when propagating information against the mesh diagonal. Reconstruction allows the higher order scheme to recover more than the single order of magnitude associated with the slope estimation and very nearly matches the discrete solutions of the quadrilaterals and equilateral triangles. By enlarging the stencil to incorporate data in the face-normal direction, reconstruction reduces the misalignment of the Riemann problem present in the first order discrete solutions.

Some general comments stem from this investigation with the unlimited schemes on regular meshes: (1) On regular meshes the Green-Gauss and least squares gradient estimation procedures yield similar results. (2) The regular quadrilateral and equilateral meshes yield very similar discrete solutions, both in order of accuracy, and absolute magnitude of the error. Nevertheless, the simulations on quadrilaterals require approximately 50% less storage and CPU simply by virtue of the fact that fewer edges exist in the domain. (3) The scheme seems to treat right triangles as distorted equilateral triangles, and increases the reliance on the gradient estimation for the production of accurate discrete solutions.

### 3.2.3 Limiter Behavior

The next set of numerical examples introduces the slope limiters into the simulations on the three sets of regular meshes previously presented. This investigation is designed to quantitatively compare the effects of limiting on scheme accuracy with each of the three polygons types.

As mentioned earlier, the limiter originally proposed for the scheme [1] is a scalar correspond-



ing to the severest requirement which maintains monotonicity. The directional implementation of this limiter was presented in Section 2.2 and is designed to reduce the severity of the limiting by decreasing only the normal component of the gradient. The third limiter examined was recently proposed by Venkatakrishnan [7]. This smooth limiter is less severe, and is invoked less frequently than Barth's original limiter.

After converging numerical simulations on the medium quadrilateral mesh for about 10,000 iterations to reach a steady state, the behavior of the limiter with each scheme was monitored for several hundred iterations. Table 1 contains an excerpt from this data and tracks the mean behavior of each limiter for several iterations. The first two columns display the percentage of all edges within the domain on which the limiter was applied for each reconstruction method. The last two columns tabulate the average value of the limiter on only those faces where the limiter was active, thus giving a picture of the severity of the limiting taking place. Of course, since the discrete answers are slightly different, the edges with flux evaluations that invoke the limiter are not always the same from solution to solution. The lack of absolute convergence with Barth's limiter is immediately apparent in the first two columns as the number of limited edges changes from time step to time step but hovers around 17%. The average value of the limiter on these edges is around 0.25 indicating a very nearly first order flux evaluation on these edges. Applying this limiter only to the normal component of the gradient substantially reduces the magnitude of the slope degradation as shown by the tabulated results with the directional limiter. With this vector application of Barth's limiter, the limited slopes retain 92 – 94% of their magnitude and monotonicity is still guaranteed. The fact that the exact number of limited edges is now substantially more stable gives evidence of the deeper convergence afforded by the milder limiting. Venkatakrishnan's limiter is designed to fire less frequently, and this table shows that with  $K = 10$  it is triggered on only 5 – 6% of the edges depending on the reconstruction, and reduces the slopes by an average of only 2 – 3%.

Figure 10 summarizes the effects of limiting on the order of accuracy with the regular

Table 1: Table showing severity and frequency of limiter firing after practical convergence – average values on medium mesh for supersonic vortex flow

**Barth's limiter**

% edges limited		Mean $\Psi$	
GG	LS	GG	LS
18.32677	16.62402	0.2444862	0.2487914
17.01772	15.99409	0.2593847	0.2473031
16.63386	18.34646	0.2549107	0.2249657
19.19291	16.70275	0.2311892	0.2505058
17.70669	15.86614	0.2648712	0.2523419
16.80118	17.42126	0.2390375	0.2494676
18.58268	15.75787	0.2293676	0.2628614
17.14567	15.59055	0.2513207	0.2808488
16.68307	17.02756	0.2457611	0.2357707
18.24803	15.93504	0.2329683	0.2580887

**Directional limiter**

% edges limited		Mean $\Psi$	
GG	LS	GG	LS
24.72441	24.58661	0.9240345	0.9457827
24.72441	24.57677	0.9240335	0.9457660
24.72441	24.57677	0.9240359	0.9457663
24.72441	24.57677	0.9240357	0.9457676
24.72441	24.55709	0.9240360	0.9457363
24.72441	24.56693	0.9240357	0.9457521
24.72441	24.56693	0.9240364	0.9457527
24.72441	24.56693	0.9240357	0.9457538
24.72441	24.54725	0.9240348	0.9457356
24.72441	24.56693	0.9240317	0.9457530

**Venkatakrishnan limiter,  $K = 10$**

% edges limited		Mean $\Psi$	
GG	LS	GG	LS
6.072834	4.970472	0.9779245	0.9867367
6.072834	4.970472	0.9779246	0.9867366
6.072834	4.970472	0.9779246	0.9867365
6.072834	4.970472	0.9779242	0.9867367
6.072834	4.970472	0.9779242	0.9867365
6.072834	4.970472	0.9779242	0.9867368
6.072834	4.970472	0.9779245	0.9867368
6.072834	4.970472	0.9779246	0.9867369
6.072834	4.970472	0.9779245	0.9867367
6.072834	4.970472	0.9779245	0.9867367

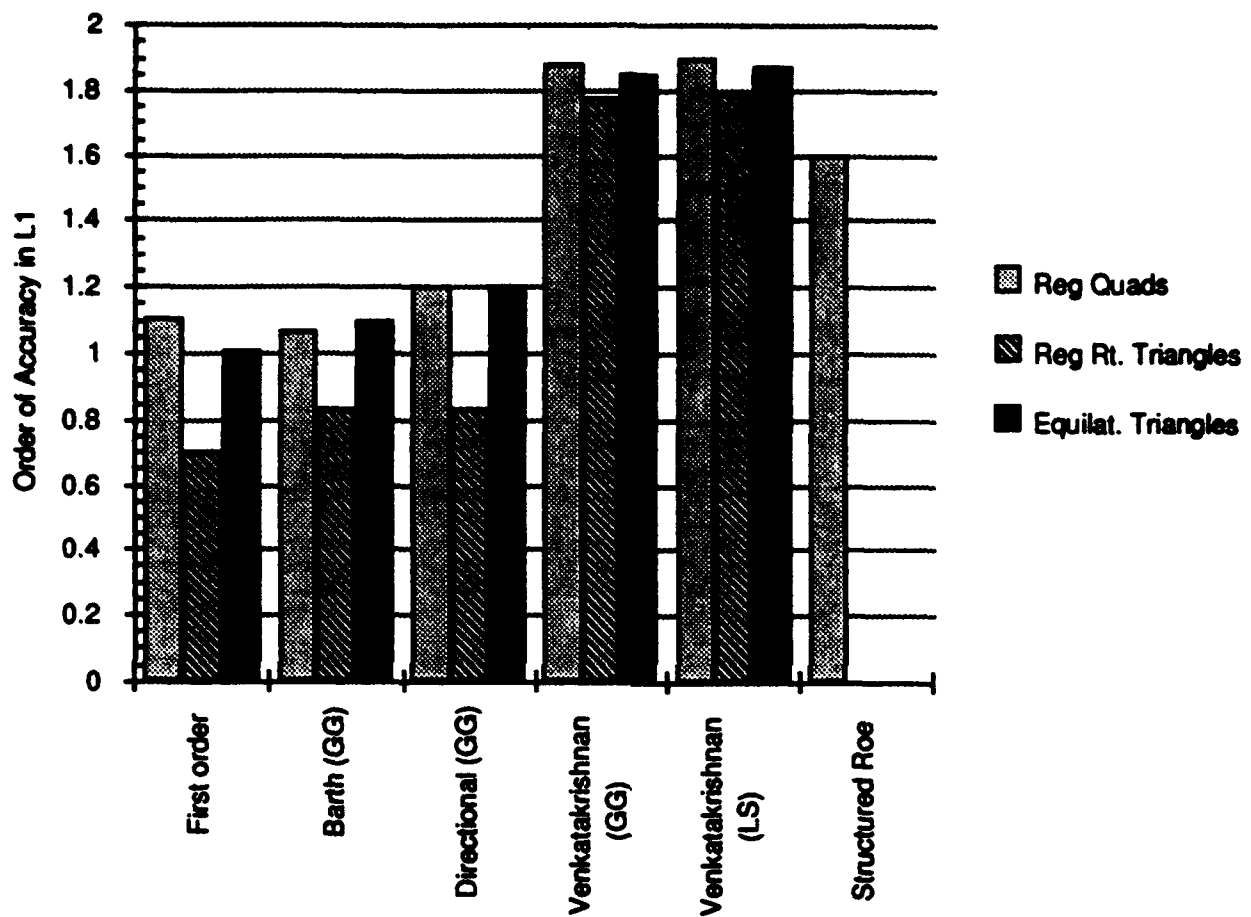


Figure 10: Order of accuracy of limited schemes on regular polygons for the supersonic vortex problem

meshes of each polygon shape. These results summarize the data contained in Table A.2 in the Appendix which presents both error norms and order of accuracy estimates. Figure 10 shows that Venkatakrishnan's limiter nearly reproduces the behavior of the unlimited schemes for this smooth flow. This is consistent with the high values of the limiter observed in Table 1.

In cases with no limiting, or with very little limiting - as with Venkatakrishnan's limiter - the right triangular elements almost match the accuracy of the other two tessellations. However, this has come from an increased reliance on the gradient estimation. The behavior with the directional limiter provides a good demonstration of this. When the gradient at  $L$  or  $R$  is decreased due to limiting, the stencil will again revert to the poorly aligned first order Riemann solution and the propagation of information will be restricted. Thus, the reconstructed values at the cell face will degrade rapidly. In Equation 2.13, accurate estimations of  $\phi_{r,m}$  rely ever more heavily on  $\nabla\phi$  since  $\phi_{V_0}$  represents data not normal to the face. Thus, limiting  $\nabla\phi$  will degrade the discrete solution more severely than on well aligned meshes. On the finest right triangular mesh with the directional limiter the error is nearly 10 times that on the equilateral triangles or quadrilaterals with the same limiter (see Table A.2 in Appendix).

### 3.2.4 Polygon Quality

While it is informative to evaluate the scheme performance on the meshes in the previous investigation, such smooth, regular, aspect ratio  $\sim 1$  polygons are rarely found in practice. Having established a reference level for scheme accuracy, focus now shifts to discrete solutions on stretched and distorted meshes.

Figure 11 displays two sets of telescoping stretched meshes. The quadrilateral and triangular elements were formed on the same set of vertices and the aspect ratio of the (quadrilateral) elements is about 40. The original scalar limiter, and the directional limiter refused to converge on the coarse and medium triangular meshes for this case, so Table A.2 in the Appendix only contains results with the first order scheme and Venkatakrishnan's limiter.

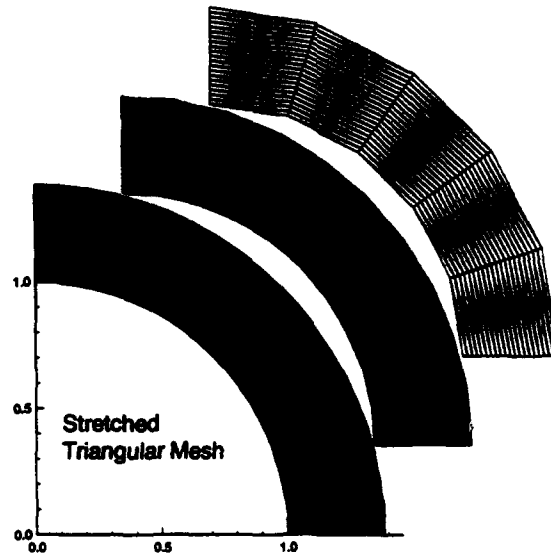
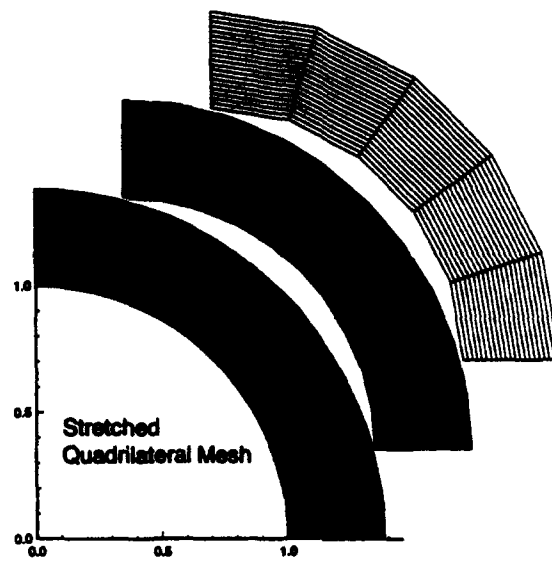


Figure 11: Sequences of stretched meshes used for supersonic vortex

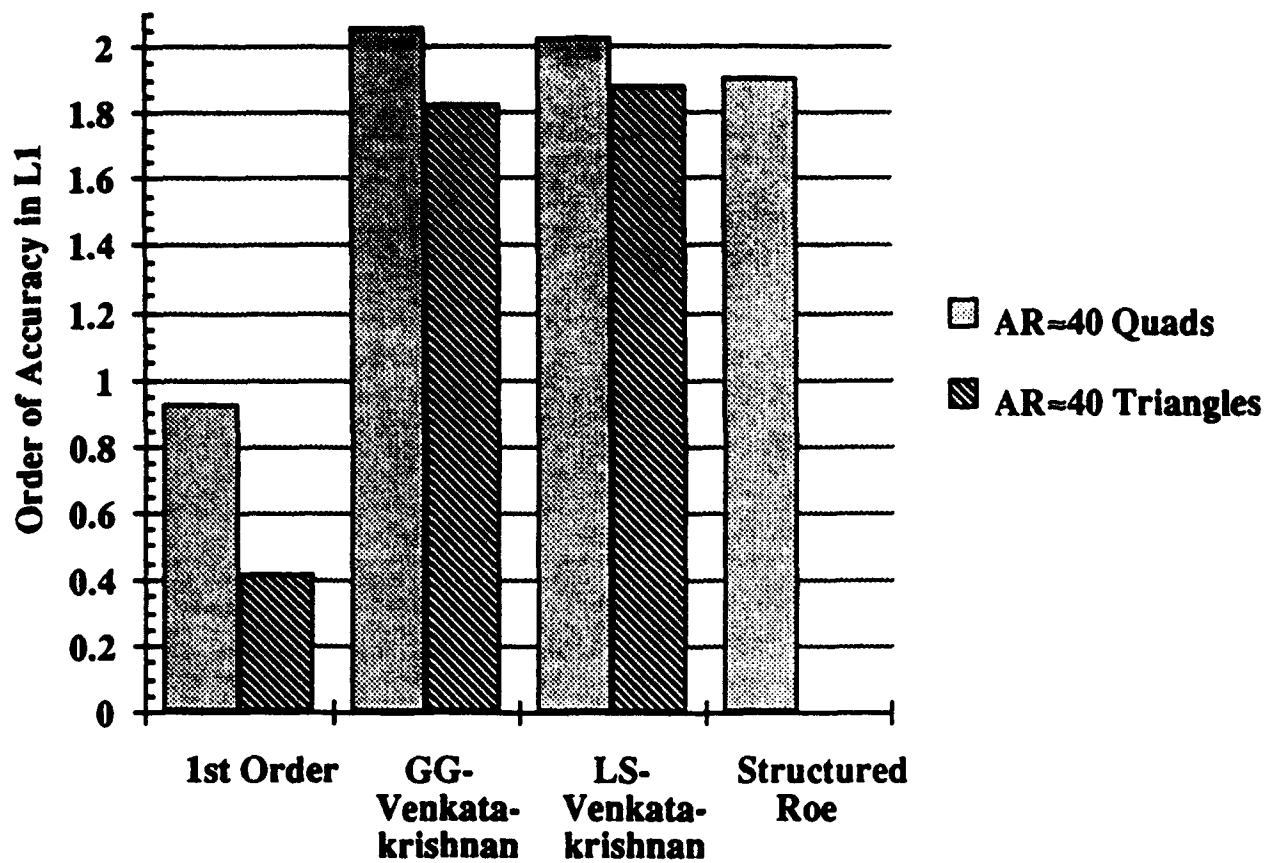


Figure 12: Order of accuracy of limited schemes on stretched polygons for the supersonic vortex problem

Figure 12 contains a comparison of the order of accuracy information derived from the tabulated data. The first order results place the order of accuracy on the quadrilateral cells at 0.93 and the right triangular scheme at only 0.41. Such results are consistent with the argument presented earlier which predicted that the alignment problem becomes worse with increasing cell aspect ratio.

At first glance, the improvement in order of accuracy for the reconstructed solutions on the triangular grid is very impressive. Although the order of accuracy is still 5 – 10% lower than on the quadrilateral meshes, reconstruction has improved the solution by more than a full order of magnitude. However, after examining the data in Table A.3, it is clear that even on the finest mesh, the discrete solutions on the right triangular mesh exhibit 4 – 10 times more error than on the quadrilateral tessellation of the same set of nodes. Despite this, the discrete solutions on the fine triangular mesh are quite reasonable, and on a sufficiently fine mesh, the gradient estimation is able to compensate for the error in the first order scheme.

The right triangle's increased dependency on the accuracy of the gradient estimation becomes apparent when studying the behavior of the discrete solutions on the coarse meshes. On these meshes, only 5 points spanned the domain in the streamwise direction. The resulting gradient estimates led to discrete solutions which are actually worse than the first order simulations. On the quadrilateral meshes, similar gradient estimates improved the discrete solutions by a factor of 2 – 6.

Finally, in regarding Table A.3, note that the discrete solution on the right triangular mesh using least squares reconstruction converged to a result which unstated the flow. Since it converged to a different physical solution, this point was not considered in the slope estimate provided in the table. The results for this test case appear to substantiate observations made previously. However, the schemes poor performance on the coarse right triangular mesh suggests that they should be regarded as preliminary until the results can be substantiated by computations on still finer stretched meshes.

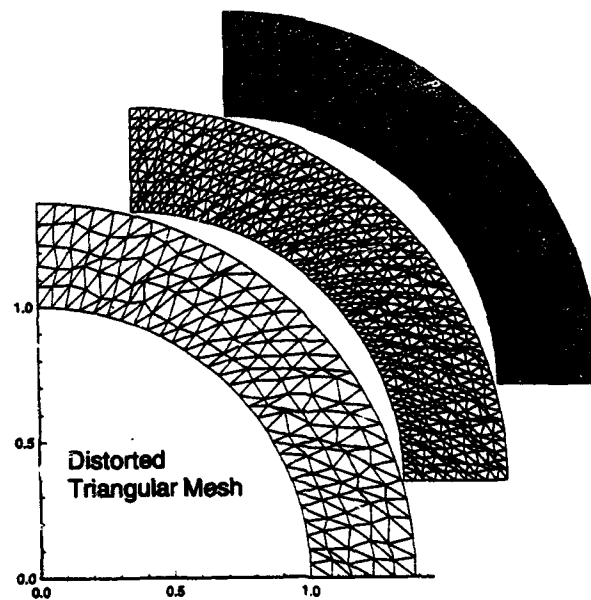
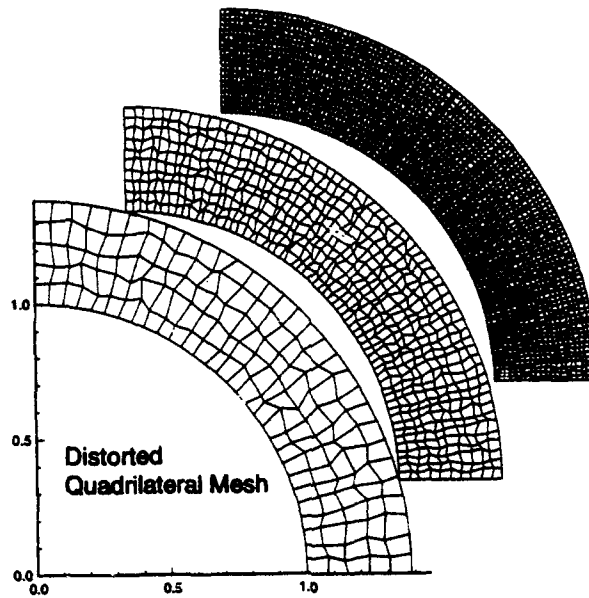


Figure 13: Sequences of randomly distorted meshes used for supersonic vortex



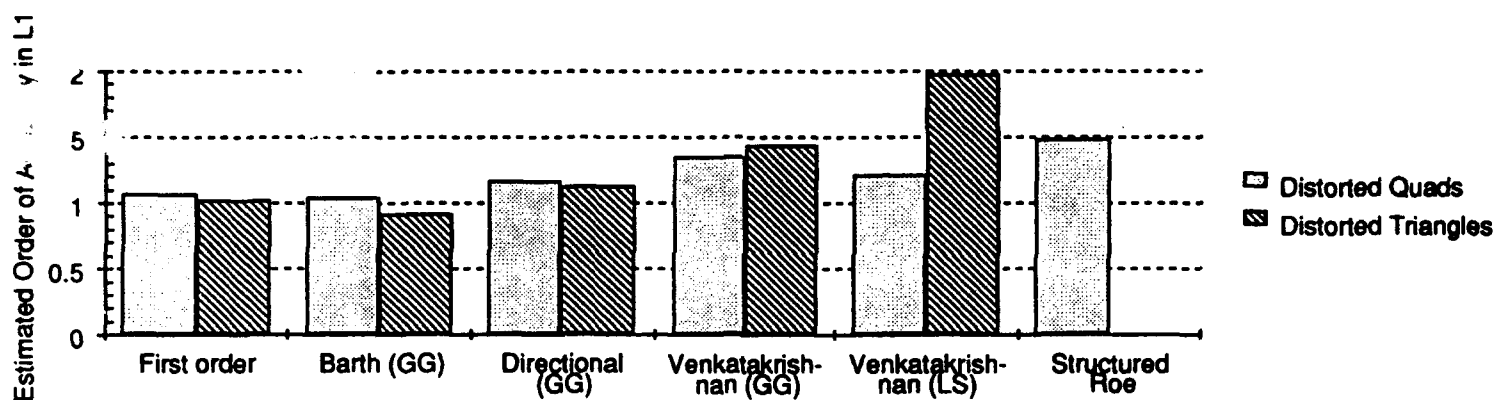


Figure 14: Order of accuracy of limited schemes on randomly distorted polygons for the supersonic vortex problem

In order to examine the schemes tolerance to distorted elements, the regular meshes shown in Figure 5 were perturbed to introduce localized skewing. Figure 13 displays the resulting distorted meshes. Each mesh point was randomly displaced within a small region of its local neighborhood. The resultant sets of nodes were then connected to form both quadrilateral and triangular polygons. Notice that these meshes do not telescope, since the magnitude of the mesh point displacement scales with the normalized mesh spacing.

Figure 14 compares the estimated order of accuracy for each discrete method on the two polygon types. This chart is again drawn from the information provided in the Appendix (Table A.4). The chart displays a clear degradation in accuracy on the quadrilateral meshes. The triangular elements, in contrast, produce results which nearly match those on regular equilateral triangles presented earlier. Table A.4 shows that, in general, somewhat higher discretization error exists on the distorted triangular meshes. However, this table also shows that the least squares cases are extremely tolerant to the mesh distortion and the error in these solutions is very nearly as low as that on the regular triangular meshes.

These observations support several general statements about the method's performance on distorted polygons. It appears that on both tessellations, the least squares gradient estimation is far more capable of producing reliable results on distorted meshes. Moreover, its also evident that the trapezoidal integration of the Galerkin portion of the numerical flux function on triangles makes these polygons far more tolerant of mesh distortion. The order of accuracy on the distorted quadrilateral meshes degenerates much more quickly, since the edge formulas only result in midpoint quadrature for these polygons. Notice however, that the absolute magnitude of the error on all of the quad meshes remains very low which suggests that the coefficient of the discretization error expression remains small.

### 3.3 External Inviscid Flow - Transonic NACA 0012 Airfoil

Transonic, inviscid flow past a NACA 0012 airfoil poses a challenging and realistic problem on which to verify the features of the various algorithms discussed in the preceding sections. Mach 0.8 flow at an angle of attack of  $1.25^\circ$  results in a steady solution with a slip line at the trailing edge, a strong shock on the suction surface, and a weak shock on the pressure side. The upper and lower frames on the left of Figure 15 show the quadrilateral and triangular meshes (respectively) used in the simulation. The remainder of this figure contains a sampling of typical results for several combinations of limiter and reconstruction method. Results on the quadrilateral control volumes are displayed above the discrete solutions on the triangular meshes.

The mesh employed in this example consists of  $131 \times 65$  vertices, and the circumferential resolution was chosen such that the lower shock just formed when using the Green-Gauss reconstruction in conjunction with Venkatakrishnan's limiter, on the quadrilateral mesh. The second column in Figure 15 contains the first order discrete solutions on each mesh. As in the previous examples, the first order triangular scheme produces a result which appears more diffuse than that on the quad mesh. The triangles near the surface are very nearly right triangles with an aspect ratio of roughly 10, and the most likely explanation is again poor alignment of the Riemann solver.

The last 2 columns of Figure 15 display reconstructed solutions using the directional limiter with Green-Gauss and Venkatakrishnan's limiter with least squares. Reconstruction dramatically improves the quality of the discrete solutions not only because of the higher order of accuracy of the resulting scheme, but also as a result of the extended support stencil used in forming the Riemann problem. Ultimately, the discrete solutions on the two meshes are extremely close. In fact, with Venkatakrishnan's limiter and least squares reconstruction, the solutions with the quadrilaterals and the triangles are very nearly indistinguishable and the lift coefficients match to 3 significant digits.

The  $C_p$  plots in Figure 16 provide a more quantitative assessment of the different schemes. This figure contains the results from all tested combinations of limiter and reconstruction method.

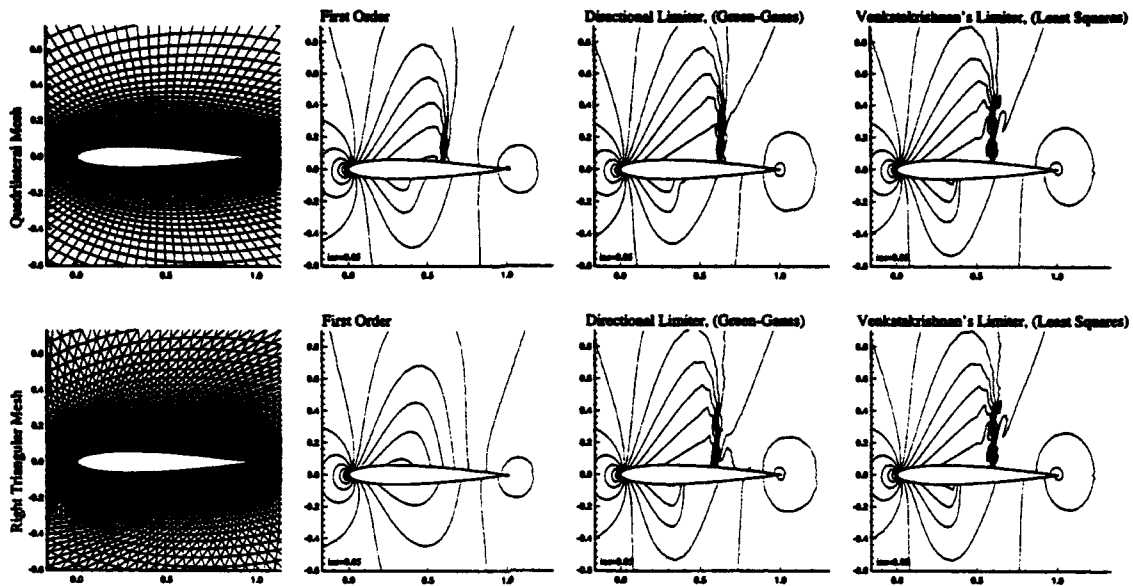


Figure 15: Meshes and isobars for a sampling of typical discrete solutions for a NACA 0012 at  $M_\infty = 0.8$  and  $\alpha = 1.25$  deg. (upper - quadrilaterals, lower - triangles,  $131 \times 65$  mesh)

Also included for reference are results from a cell-centered structured Roe/MUSCL solver [21]. The profiles are strongly dependent upon the capturing of the weak lower shock. Less accurate methods fail to predict this shock and represent it as simply a smooth compression. With the exception of the structured mesh results, hollow squares denote data with the quadrilateral meshes, while filled triangles represent the triangular elements.

In the first order solutions, only the quadrilateral mesh gives any indication of the lower shock's existence. On either of these meshes, the original scalar limiter fails to predict the shock as well. Indeed, these results did not converge convincingly, and the residual stalled after dropping approximately 3 orders of magnitude. The directional implementation of this limiter reduced the residual by an additional two orders, and the lower shock is evident in the discrete solutions on both tessellations. As in the previous examples, Venkatakrishnan's limiter converges to machine zero, but over/undershoots appear in all the examples.

The behavior of the two reconstruction methods follows the same trends as in the shockless flows considered earlier. Least squares appears to produce more accurate gradient estimates, and the advantage is particularly evident on the triangular meshes. This method also shows a reduced sensitivity to polygon shape because it more appropriately weights the data surrounding a vertex. On triangular meshes formed by division of quadrilaterals, the Green-Gauss reconstruction may actually introduce a diagonal bias, while the least squares reduces the weighting of these points due to their distance from the central vertex. On none of these relatively smooth grids did the additional edge calculations present on the right triangular meshes result in any apparent advantage.

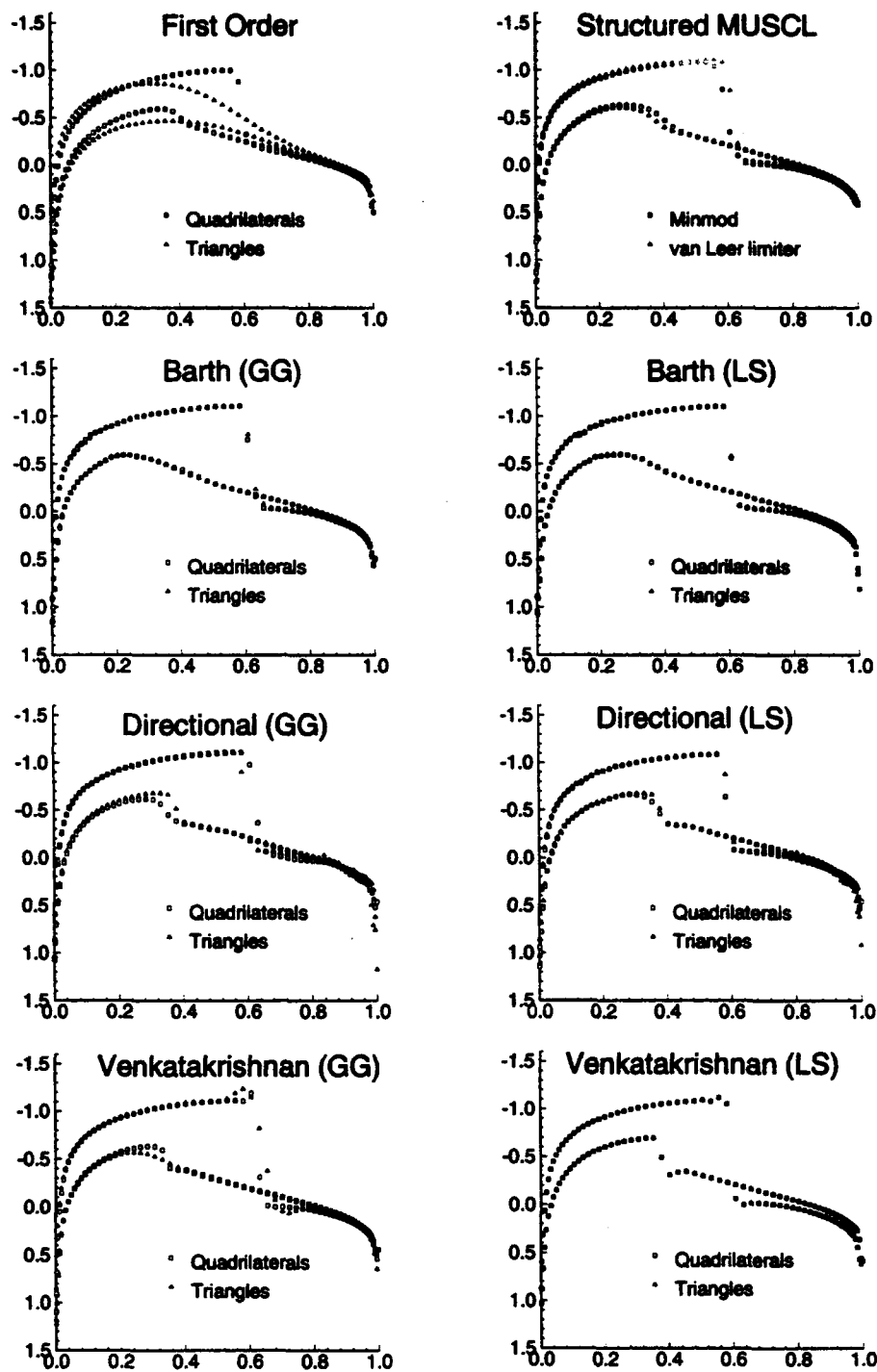


Figure 16:  $C_p$  distributions with various schemes for Mach 0.8,  $\alpha = 1.25^\circ$  NACA 0012 airfoil

## 4. Conclusions

The accuracy and efficiency of a variety of common edge-based reconstruction schemes are examined on unstructured meshes with various limiters and types of polygons. For meshes with cell aspect ratios near one, the accuracy of the discrete solutions on triangles and quadrilaterals is nearly the same in both order and absolute magnitude. Right triangular elements, however, appear to be viewed as distorted equilateral triangles - with an associated reduction in scheme accuracy which is particularly severe in the piecewise constant, first order scheme. The situation is exacerbated when the mesh is stretched to produce high aspect ratio elements and the Riemann solver is more poorly aligned with the edge which introduces the first order data. Higher-order calculations on such meshes rely on the reconstruction to extend the support of the first order stencil. This results in an increased burden on the gradient estimation, and makes them easily degraded by limiting. Even when the reconstruction helps recover the loss in order of accuracy, the absolute level of error in the discrete solutions remains a factor of 5-10 higher than on the quadrilateral meshes. The fact that quadrilaterals are not rigid figures makes it possible to stretch these cells without introducing skewing, and elevated cell aspect ratio does not degrade these discrete solutions. Nevertheless, on poor quality meshes, the midpoint integration and smaller support stencil of the quadrilateral meshes combine to make the discrete solutions degenerate more rapidly.

A new directional implementation of Barth's original scalar limiter is introduced which preserves the cell average and retains monotonicity. This approach limits only the component of the gradient normal to the face. Numerical experiments show that this implementation significantly reduces the dissipation introduced by the original scalar procedure. Venkatakrishnan's smooth limiter performs as expected and converges for all test cases while producing small over/undershoots in the discrete solutions. A very promising approach toward further reducing the introduction of excessive dissipation into the solutions may be the directional implementation

of Venkatakrishnan's limiter.

On regular and stretched meshes, the additional edges in the triangular meshes do not lead to any apparent accuracy advantage over the quadrilateral scheme. These additional edges, however, do mandate 50% higher (in 2-D) storage and CPU requirements (over 200% in 3-D) - simply by virtue of the tessellation and the fact that the scheme proceeds on an edge basis. These observations support a possible mesh generation strategy which removes unnecessary edges from boundary layer regions and other regular portions of an unstructured triangular mesh, and processes such regions as a collection of mixed quadrilateral and triangular elements.



## 5. References

- [1] T.J. Barth and D.C. Jespersen. The Design and Application of Upwind Schemes on Unstructured Meshes. *AIAA Paper 89-0366*, January 1989.
- [2] M. Aftosmis and N. Kroll. A Quadrilateral-Based Second-Order TVD Method for Unstructured Adaptive Meshes. *AIAA Paper 91-0124*, January 1991.
- [3] N.T. Frink, P. Parikh, and S. Pirzadeh. A Fast Upwind Solver for the Euler Equations on Three-Dimensional Unstructured Meshes. *AIAA Paper 91-0102*, January 1991.
- [4] A.A. Fursenko, D. M. Sharov, E.V. Timofeev, and P.A. Voinovich. High-Resolution Schemes in Unstructured Grids in Transient Shocked Flow Simulation. *Lecture Notes in Physics, 13th International Conference on Numerical Methods in Fluid Dynamics*, Springer Verlag, (414):250-255, 1993.
- [5] A. Harten. High Resolution Schemes for Hyperbolic Conservation Laws. *Journal of Computational Physics*, 49:357-393, 1983.
- [6] B. van Leer. Flux-Vector Splitting For the Euler Equations. Technical Report 82-30, ICASE, September 1982.
- [7] V. Venkatakrishnan. On the Accuracy of Limiters and Convergence to Steady State Solutions. *AIAA Paper 93-0880*, January 1993.
- [8] T.J. Barth. A 3-D Least Squares Upwind Euler Solver for Unstructured Meshes. *Lecture Notes in Physics, 13th International Conference on Numerical Methods in Fluid Dynamics*, Springer Verlag, (414):240-244, 1993.
- [9] T.J. Barth. Aspects of Unstructured Grids and Finite-Volume Solvers for the Euler and Navier-Stokes Equations. Technical report, AGARD Report 787, 1992.

- [10] T.J. Barth. Recent Developments in High Order K-Exact Reconstruction on Unstructured Meshes. *AIAA Paper 93-0668*, January 1993.
- [11] L.J. Durlofsky, B. Engquist, and S. Osher. Triangle Based Adaptive Stencils for the Solution of Hyperbolic Conservation Laws. *Journal of Computational Physics*, 98:64-73, 1992.
- [12] M. Aftosmis. Viscous Flow Simulation Using an Upwind Method for Hexahedral Based Adaptive Meshes. *AIAA Paper 93-0772*, 1993.
- [13] T.J. Barth. Numerical Aspects of Computing Viscous High Reynolds Number Flows on Unstructured Meshes. *AIAA Paper 91-0721*, 1991.
- [14] T.J. Barth and P.O. Frederickson. Higher-Order Solution of the Euler Equations on Unstructured Grids Using Quadratic Reconstruction. *AIAA Paper 90-0013*, 1990.
- [15] A.G. Godfrey, C.R. Mitchell, and R.W. Walters. Practical Aspects of Spatially High Accurate Methods. *AIAA Paper 92-0054*, 1992.
- [16] W.J. Coirier and K.G. Powell. An Accuracy Assessment of Cartesian-Mesh Approaches for the Euler Equations. *AIAA Paper 93-3335-CP*, 1993.
- [17] R.H. Ni. A Multiple-Grid Scheme for Solving the Euler Equations. *AIAA J.*, 20:1565-1571, 1982.
- [18] E. Boxer, J.R. Sterrett, and J. Wlodarski. Application of Supersonic Vortex-Flow Theory to the Design of Supersonic Impulse Compressor- or Turbine-Blade Sections. *NACA RM L52B06*, 1952.
- [19] L.J. Goldman and V.J. Scullin. Analytical Investigation of Supersonic Turbomachinery Blading I. Computer Program for Blading Design. *NASA TN D-4421*, 1968.

- [20] T.S. Tavares. A Supersonic Fan Equipped Variable Cycle Engine for a Mach 2.7 Supersonic Transport. *NASA-CR-177141*, 1986.
- [21] D. Gaitonde and J. Shang. Accuracy of Flux-Split Algorithms in High-Speed Viscous Flows. *AIAA J.*, 31(7):1215–1221, 1993.